Planar, Ablative Rayleigh-Taylor Instability Growth in Copper Foils Driven by Nova Hohlraum Radiation

G. T. Schappert, S. E. Caldwell, W. W. Hsing (P-24), D. E. Hollowell (XTA)

The Rayleigh-Taylor (R-T) instability is an instability of the interface between two materials when a lighter material pushes on and accelerates a heavier material. This situation can occur in implosions of inertial confinement fusion (ICF) capsules as well as in stellar dynamics in astrophysics. Of particular interest is the ablative R-T instability, in which the lower-density ablated material accelerates the bulk material through a rocket effect. The theory for this case was worked out some time ago, leading to an exponential growth rate γ for a perturbation in the ablation surface. This rate depends on the wave number of the perturbation, the scale length of the density gradient across the ablation front, the acceleration of the interface, and the mass-ablation rate. The instability growth rate for the ablatively driven acceleration is less than the classical growth rate (without ablation) under otherwise identical conditions. This reduced rate of instability growth is referred to as ablative stabilization.

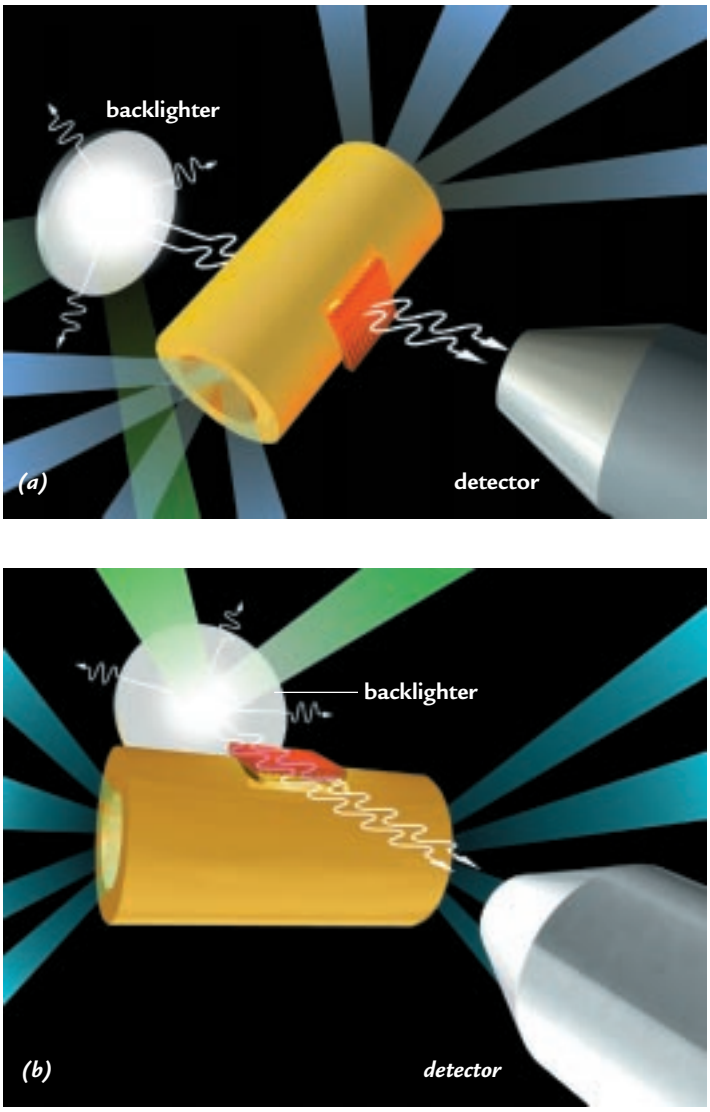

Fig. II-24. The experimental layout for (a) face-on radiography and (b) edge-on shadowgraphy, showing the eight Nova drive beams in blue, the two backlighter beams in green, the hohlraum in gold, the copper foil in red, and the x-rays that are emitted from the backlighter.

The purpose of our research is to experimentally explore the ablative R-T instability in a high-density material and obtain results that can be modeled by various laboratory codes, thus benchmarking these codes with real experiments. The R-T experiments were performed at the Nova laser at Lawrence Livermore National Laboratory. The material that we investigated was copper, and the ablative drive was the ~180-eV radiation density generated in a scale-1 hohlraum. Two distinct experimental configurations were used: one with face-on radiography to measure perturbation growth, the other with edge-on shadowgraphy imaging of the growth. Both configurations used 6.7-keV x-rays. The two layouts are shown in Fig. II-24, and they are described in detail below.

Eight of the ten Nova laser beams (each with a wavelength of 0.351 μm [3ω], a pulse length of 2.2 ns, and an energy of about 3 kJ) were focused into the cylindrical hohlraum to generate the radiation drive of about 180 eV. The other two beams (each with a wavelength of 0.527 μm [2ω], a pulse length of 2–4 ns, and an energy of 3–4 kJ) were passed through random-phase plates to produce fairly smooth focal spots with diameters of about 500 μm on a 2-mm-diameter, 18-μm-thick iron disk. These beams generated 6- to 8-keV helium-like iron lines. This iron backlighter was used for both radiography and shadowgraphy. X-ray imaging devices were filtered with a 0.5-mil, cold-iron foil to remove the higher-energy lines and leave only the $1s^2$-$1s2p$ He_α line at 6.7 keV.

The hohlraums were standard scale-1 gold cylinders that were 2750 μm long and 1600 μm in diameter, with a 25-μm wall thickness and 75%-open end caps for laser-beam entrance holes. The copper targets were mounted over a hole in a slightly flattened region of the cylinder. For face-on radiography, a second hole in the cylinder diametrically across from the target let the backlighter radiation traverse the hohlraum and the target. The target was an 18-μm-thick flat copper foil with 45- or 80-μm-wavelength, 0.5-μm-amplitude sinusoidal corrugations milled on one side. A 600-μm × 600-μm square with the corrugations facing inward was mounted across the opening in the hohlraum.

For face-on radiography (Fig. II-24a), the target was imaged with a gated x-ray imager (GXI) along a line of sight that was normal to the target and that continued through the target and hohlraum to the center of the iron backlighter disk behind the hohlraum. The GXI produced 16 pinhole images in groups of four. Within a group, the images were separated by about 60 ps, and the time separation between groups was adjustable. The temporal resolution of the GXI was about 100 ps; the growth indicated in each image was averaged over that time. Each image then recorded the transmission of the 6.7-keV backlighter x-rays through the foil. The growth of the periodic perturbation caused by the R-T instability in the foil was mapped onto a periodic contrast variation in the GXI image, as shown in Fig. II-25. Also shown in Fig. II-25 is a line-out across the contrast corrugations. The oscillations at the fundamental wavelength and the appearance of a second harmonic are superimposed on the shape of the backlighter image.

The line-out for each image was analyzed, and the temporal development of the foil perturbation growth was reconstructed. The three major steps in this analysis are the subtraction of the backlighter image, Fourier analysis of the periodic perturbations, and correction of the Fourier components for the spatial resolution of the instrument. The amplitudes of the corrected Fourier

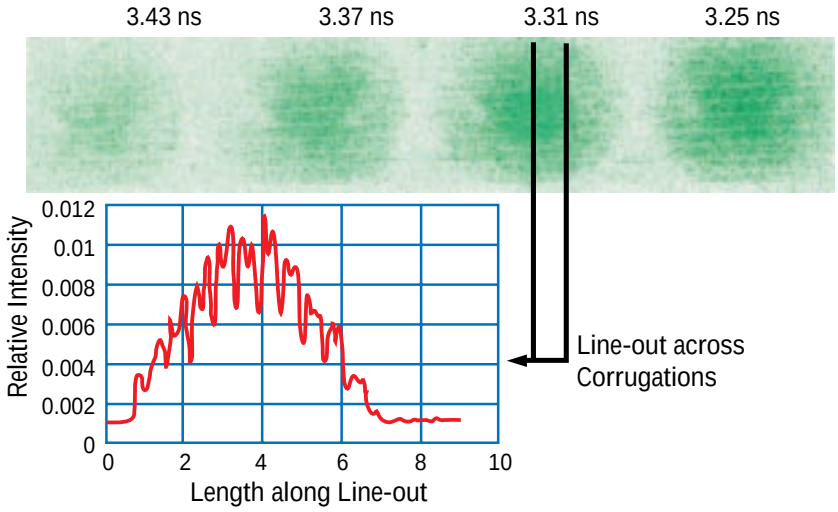

Fig. II-25. A time sequence of radiographs from a gated x-ray imager.

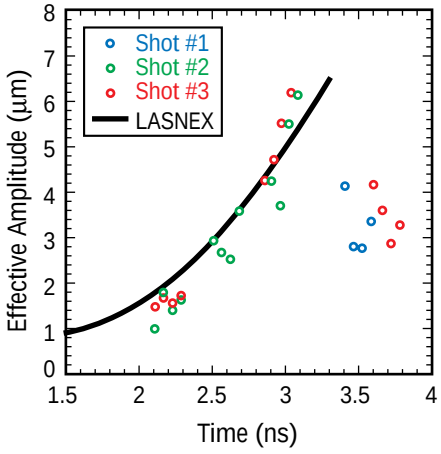

(a)

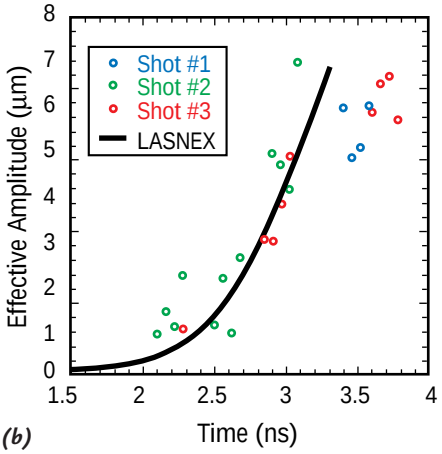

(b)

Fig. II-26. (a) The growth of the fundamental wavelength for the 45-μm corrugation. (b) The growth of the second harmonic for the 45-μm corrugation. The colors of the data points correspond to three different shots.

components reflect the growth of the contrast, that is, the integral of $\kappa\rho(x)\mathrm{d}x$ through the foil, where κ is the absorption coefficient of cold copper at 6.7 keV and ρ is the density. Although the copper was heated, the absorption at 6.7 keV is nearly the same as that for cold copper. Dividing the contrast amplitude by the cold-copper absorption coefficient gives an effective spatial amplitude based on cold, normal-density copper.

Figure II-26 shows this amplitude as a function of time for the 45-μm-wavelength perturbation and its second harmonic at 22.5 μm, respectively. The initial 0.5-μm amplitude of the fundamental wavelength is too small to give an observable contrast, and the second harmonic starts from zero amplitude since it was not initially present in the foil. The data for the fundamental wavelength show an initial exponential growth followed by an abrupt drop. This sharp drop is not fully understood. One would expect a gradual saturation of the amplitude followed by a decrease of all the harmonic amplitudes as the bubble-and-spike plasmas homogenize. Because the scatter in the data indicates fairly large error bars, the data could be consistent with a gradual saturation followed by a gradual drop.

Also shown in Fig. II-26 is a planar, two-dimensional LASNEX calculation (a calculation using an ICF design code) of the R-T growth using the Nova hohlraum drive. Considering the scatter of the data, the agreement is quite good for the earlier times. For later times, the calculation runs into numerical problems, which are being addressed. Results for the 80-μm corrugation foils showed slower growth and poorer agreement with our simulations. A shortcoming of this technique is that the contrast modulation in the GXI image does not directly reflect the spatial development of the perturbation in the foil but only the integral through the material. The bubble-and-spike formation in the later stages of R-T growth is observed indirectly as the appearance and growth of the second harmonic and, presumably, as higher harmonics if the instrument spatial resolution is sufficient. To observe this aspect of the R-T instability, we imaged the R-T growth in an edge-on configuration (Fig. II-24b).

The target was again mounted across an opening in the slightly flattened side of the hohlraum, offset with two 50-μm spacers. The line of sight was edge-on, down the length of the corrugations onto the center of the backlighter disk, which was also visible between the two spacers and the hohlraum and target. Two imaging techniques were used in this configuration. A GXI was used to image the growth of the corrugations directly edge-on. The bubble-and-spike formation at about 3.6 ns in an 80-μm-wavelength

corrugated foil is shown in Fig. II-27. The bright region in the lower half of the image is the direct view of the backlighter disk. The shadow of a 25-μm-diameter, gold-wire fiducial is seen in the lower right. The shadow of the lower edge of the copper foil and the spikes toward the top are clearly visible. In this case, the 6.7-keV backlighter x-rays propagated down the 600-μm-long channels of bubbles and spikes, resulting in the dark spikes and lighter bubbles. The light stripe near the top of the image is a view of the backlighter through the 50-μm offset between the foil and the hohlraum. We suspect that the dark region above the bubble-spike region and below the offset is foil plasma from the edges of the foil that were left behind in the drive because the foil was somewhat larger than the opening in the hohlraum. We plan to repeat these shots with foils mounted such that the front and back edges are well inside the opening.

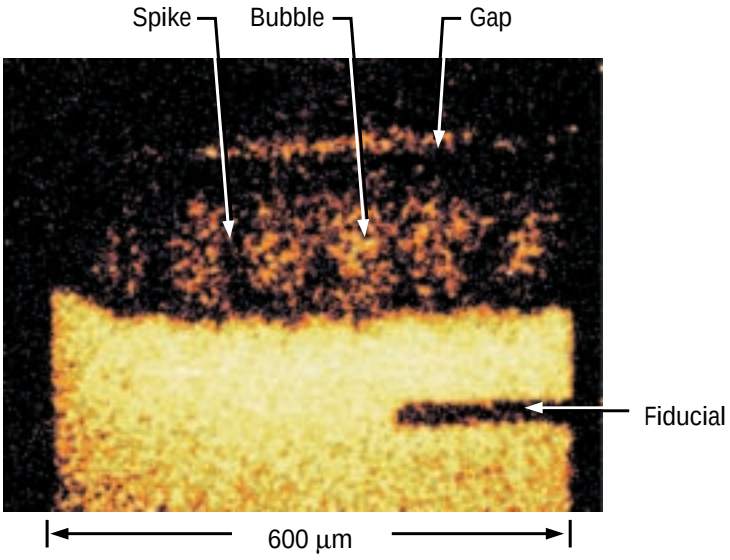

Fig. II-27. A side-on image of the bubbles and spikes.

The GXI images at various time steps can be analyzed to determine the net motion of the foil away from the hohlraum. A more precise measurement of the motion can be made with a streak camera. There is, however, a difference. The GXI image is in two dimensions, whereas the streak camera images only one. Figure II-28a shows a typical streak of the motion of a 45-μm-wavelength corrugation foil. The bright portion of the streak image is the direct view of the backlighter, showing the shadow of a fixed fiducial across the lower half of the image. The upper half shows the near-parabolic path of the back of the foil and the expanding copper plasma with the spikes and bubbles above it. Across the top in the image is the view to the backlighter through the 50-μm offset between the hohlraum and target. Figure II-28b shows the trajectories for a flat foil, for two foils with 45-μm corrugation wavelengths, and for two foils with 80-μm corrugation wavelengths. Also shown is a LASNEX calculation for a foil with a 45-μm corrugation wavelength. The agreement is quite good. There seems to be no dependence of the foil trajectory on the corrugation wavelength within the error of the measurements, considering that the time origin for the five shots is within ±100 ps, consistent with the limitations of the Nova electrical-trigger system.

The experiments discussed above are part of a laser-based, above-ground experiments (AGEX) program to study hydrodynamic instabilities. The preliminary experimental results presented are in reasonable agreement with modeling. However, better diagnostics (better in both spatial and temporal resolution), more accurate techniques for deconvolving the instrument function, and simulations that cover the whole temporal range of the experiment are required to benchmark a calculation in detail. This work is in progress.

The authors would like to thank the P-24 Nova technicians, the MST target-fabrication staff, and the Nova operations staff for their contributions to these experiments.

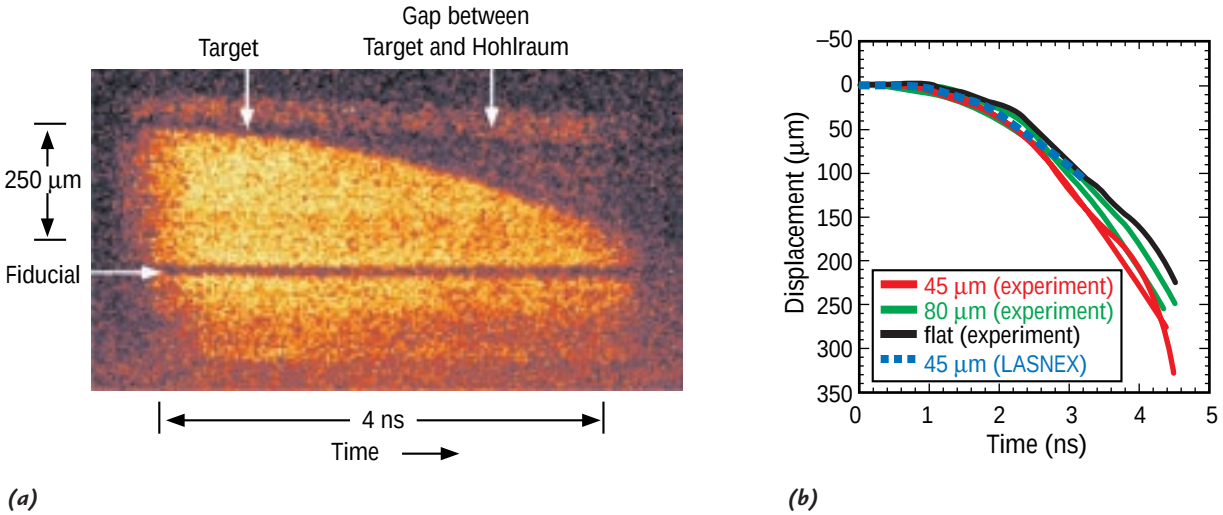

Fig. II-28. (a) The steaked motion of the back of the 45-μm corrugated target. (b) The streaked motion of the back of a flat foil and the backs of foils with 45- and 80-μm corrugation wavelengths. Also included is the LASNEX simulation for a foil with a 45-μm corrugation wavelength.